



CHORUS

This is the accepted manuscript made available via CHORUS. The article has been published as:

Imaging of Electrothermal Filament Formation in a Mott Insulator

Matthias Lange, Stefan Guénon, Yoav Kalcheim, Theodor Luibrand, Nicolas M. Vargas, Dennis Schwebius, Reinhold Kleiner, Ivan K. Schuller, and Dieter Koelle

Phys. Rev. Applied **16**, 054027 — Published 12 November 2021

DOI: [10.1103/PhysRevApplied.16.054027](https://doi.org/10.1103/PhysRevApplied.16.054027)

Imaging of electrothermal filament formation in a Mott insulator

Matthias Lange,¹ Stefan Guénon,^{1,*} Yoav Kalchheim,^{2,3} Theodor Luibrand,¹ Nicolas Manuel Vargas,² Dennis Schwebius,¹ Reinhold Kleiner,¹ Ivan K. Schuller,² and Dieter Koelle¹

¹*Physikalisches Institut, Center for Quantum Science (CQ) and LISA⁺, Eberhard Karls Universität Tübingen, Auf der Morgenstelle 14, 72076 Tübingen, Germany*

²*Center for Advanced Nanoscience, Department of Physics, University of California — San Diego, 9500 Gilman Drive, La Jolla, CA92093-0319, USA*

³*Department of Materials Science and Engineering, Technion — Israel Institute of Technology, Technion City, 32000 Haifa, Israel*

(Dated: October 15, 2021 [V2O3microscopy-manuscript-appendix](#))

Resistive-switching – the current-/voltage-induced electrical resistance change – is at the core of memristive devices, which play an essential role in the emerging field of neuromorphic computing. This study is about resistive switching in a Mott-insulator, which undergoes a thermally driven metal-to-insulator transition. Two distinct switching mechanisms were reported for such a system: electric-field-driven resistive switching and electrothermal resistive switching. The latter results from an instability caused by Joule heating. Here, we present the visualization of the reversible resistive switching in a planar V_2O_3 thin-film device using high-resolution wide-field microscopy in combination with electric transport measurements. We investigate the interaction of the electrothermal instability with the strain-induced spontaneous phase-separation in the V_2O_3 thin-film at the Mott-transition. The photomicrographs show the formation of a narrow metallic filament with a minimum width $\lesssim 500$ nm. Although the filament formation and the overall shape of the current-voltage characteristics (IVCs) are typical of an electrothermal breakdown, we also observe atypical effects like oblique filaments, filament splitting, and hysteretic IVCs with sawtooth-like jumps at high currents in the low-resistance regime. We were able to reproduce the experimental results in a numerical model based on a two-dimensional resistor network. This model demonstrates that resistive switching in this case is indeed electrothermal and that the intrinsic heterogeneity is responsible for the atypical effects. This heterogeneity is strongly influenced by strain, thereby establishing a link between switching dynamics and structural properties.

Keywords: resistive switching, electrothermal instabilities, filaments, memristive devices, Mott insulators, Vanadium(III) oxide, neuromorphic materials

I. INTRODUCTION

The strongly correlated electron system V_2O_3 is a prototypical Mott-Hubbard insulator [1]. At room temperature, stoichiometric V_2O_3 is a paramagnetic metal with corundum structure, which undergoes a metal-to-insulator-transition (MIT) in cooling below about 160 K. The insulating phase is antiferromagnetic with monoclinic structure. Upon heating, the insulating phase undergoes a thermally driven insulator-to-metal-transition (IMT) [2–4].

In recent years, there has been a growing interest in utilizing the MIT/IMT in devices based on strongly correlated oxides [5]. One area of application is optical elements, where the MIT/IMT influences the photonic properties [6, 7]. Another application area is resistive switching, where an applied electric current or field induces the IMT and changes the device’s resistance [8, 9]. Two technological problems fuel the research in resistive switching. First, there is growing interest in resistive random-access memories (ReRAMs) as next-generation, energy-efficient, non-volatile computer memories. Here, high- and low-resistive states in memristive elements

store the data [10–12]. Second, the era of “Big Data” requires methods to access huge data storage capacities efficiently, which fuels the research field of in-memory computing - combining data storage and logical operations in one chip. At the core of this technology are again memristive elements [13–15]. A sub-field of in-memory computing is neuromorphic computing - the search for physical phenomena and concepts, which allow building artificial neural networks with some of the essential functions as their biological counterparts. Again, memristive elements utilizing resistive switching play a vital role in this emerging research field [16–20].

Several mechanisms were suggested for resistive switching in Mott insulators: At very high fields ($\gtrsim 100$ MV/m) Landau-Zener tunneling across the Mott gap increases the free carrier concentration which eventually destabilizes the insulating state, leading to the IMT [21–25]. However, switching with considerably lower fields has been observed in some cases [26–28]. The low-field switching was attributed to either mid-gap tunneling [29, 30], an electric-field-driven Mott-gap collapse [31] or a spatially inhomogeneous metal-insulator mixed state [32].

In addition to these mechanisms, in materials exhibiting a thermally driven IMT, a universal electrothermal breakdown must be considered. This instability is not di-

* stefan.guenon@uni-tuebingen.de

rectly related to the Mott-Hubbard physics, but is the result of an electrothermal instability created by the strong temperature dependence of the electric resistivity at the IMT [33–36]. Such an electrothermal instability can lead to resistive switching: When current passes through a highly resistive (insulating) device, Joule heating increases the device temperature. Consequently, small spatial variations in the current density may lead to spatial variations of the local device temperature. The sharp decrease in the resistivity with increasing temperature (at the IMT) acts as a positive feedback mechanism, which amplifies the evolution of a spatially inhomogeneous state. For electric currents above a certain threshold, this may lead to a runaway effect where more and more current is concentrated in a small section of the device, considerably increasing the local temperature. This runaway effect results in the formation of a highly conductive (metallic) filament connecting the device electrodes. The filament is sustained in the metallic state by the Joule heating concentrated within it, while its surroundings remain in the insulating state at the lower base temperature. In this case, resistive switching is the result of current and temperature redistribution in the device (see Ref. 37 for an extensive discussion of this phenomenon).

Considering V_2O_3 devices, it is possible to suppress electrothermal effects and enter a purely electronic regime in ultrafast pump-probe experiments [38]. In a study on V_2O_3 nanodevices, where size effects and electrode cooling reduced Joule heating, evidence for a dielectric breakdown was found [28], and in a recent study, the authors found that defects in the V_2O_3 thin-films enhance the efficiency of field-assisted carrier generation and considerably reduce the threshold for a dielectric (non-thermal) breakdown [39]. Electrothermal switching is therefore expected in large and highly pure devices where cooling from the contacts is inefficient and defects do not play a substantial role in the switching process. Moreover, we note that due to the elastic strain and coupling between the structural and the electronic degrees of freedom, V_2O_3 thin-films on single crystal substrates have very rich physics on their own [40–42]. Of particular importance is the spontaneous phase separation with herringbone domain structures at the sub-micrometer scale due to strain minimization at the MIT/IMT [43]; this in turn is likely to also affect resistive switching at the IMT.

Despite major research efforts, details of the resistive switching mechanism remain elusive. In particular, for systems with a thermally driven IMT, the question of purely electrically vs. electrothermally induced resistive switching has been debated over recent years [9, 28, 32, 34, 35, 39, 44–47]. A fundamental problem for understanding voltage- or current-induced switching is based on the fact that in experiments the switching is analyzed by electric transport measurements. Naturally, those measurements are only sensitive to the total resistance change of the device. However, the system is inherently strongly inhomogeneous, eventually includ-

ing a strongly inhomogeneous spatial distribution of current density and temperature. Consequently, knowing the spatial distribution of those properties relevant for resistive switching is crucial. Hence, it should be highly rewarding to combine electric transport measurements with imaging of filament formation on the submicrometer scale. This may, in particular, provide so far inaccessible insights into the relation between strain-induced domain formation and switching-induced filament formation at the IMT/MIT.

In this study, we combine electric transport measurements with cryogenic optical wide-field microscopy (with a spatial resolution of about $0.5 \mu\text{m}$) on V_2O_3 thin-film devices. Due to different reflectivity, the photomicrographs yield a strong contrast between metallic and insulating regions, which allows for imaging of the metal-insulator spontaneous phase separation at the MIT/IMT and for the determination of the spatial distribution of local MIT and IMT temperatures. Furthermore, we image the evolution of the formation of highly conducting (metallic) filaments that accompany resistive switching upon sweeping an applied current in the insulating state and recording simultaneously the current-voltage characteristics (IVCs). This way, characteristics of the electric transport measurements can be related to the formation, growth and extinction of metallic filament features at the submicron scale. We find that both IVCs and photomicrographs have many characteristics of electrothermal resistive switching due to a Joule heating filament formation. However, we also observe details, which we assume to result from the interaction of Joule heating filaments with the strain-induced varying IMT/MIT temperatures. We developed a numerical model based on a two-dimensional resistor network, which takes into account the experimentally determined spatial distribution of the local MIT/IMT temperatures. With this model, we calculate IVCs and the spatial distribution of current density and temperature upon electrothermal resistive switching and find excellent agreement with experimentally determined IVCs and optically detected filament formation. These results provide a profound understanding of the resistive-switching-mechanism details at play. In particular, comparing the spontaneously formed metal-insulator domain structure with the filamentary structures resulting from electrothermal switching also reveals a hitherto unknown interplay between strain and switching.

This article is organized as follows: After Sec. II on sample fabrication and experimental setup, we discuss in Sec. III the thermally driven MIT/IMT in the planar V_2O_3 thin-film device under investigation. In addition to resistance R vs. temperature T data (Sec. III A), we present photomicrographs at the MIT/IMT, which show characteristic insulator-metal herringbone domain structures (Sec. III B). Then, we derive in Sec. III C maps of spatially resolved transition temperatures.

The main results are presented in Sec. IV on resistive switching by current-induced MIT. There, we show

IVCs in combination with photomicrographs at the IMT-onset (Secs. IV A and IV B) and discuss the experimental results (Sec. IV C). We then present a numerical model (Sec. IV D), based on a two-dimensional (2D) resistor network, which shows good agreement in comparison with the experimental results (Sec. IV E). Section V concludes this work.

II. SAMPLE FABRICATION & EXPERIMENTAL SETUP

A 300-nm-thick V_2O_3 thin-film was grown by rf magnetron sputtering of a V_2O_3 target on a r-cut sapphire substrate; see Ref. 48 for details. Subsequently, by an optical lithography lift-off process, we prepared several-100-nm-thick Au contact pads on top of the unpatterned V_2O_3 film, to define 12 devices on the chip. Each device consists of a $19.5\text{-}\mu\text{m}$ -long gap between two $20\text{-}\mu\text{m}$ -wide Au electrodes (see Fig. 1(a)).

We used a wide-field optical microscope [49] with the device mounted in vacuum, in a continuous He gas-flow cryostat. This configuration facilitates electrical transport measurements simultaneous with optical imaging of the device. The microscope has a spatial resolution of about $0.5\text{ }\mu\text{m}$. The illumination is monochromatic with a wavelength of 528 nm , and the field of view is $500\text{ }\mu\text{m} \times 500\text{ }\mu\text{m}$. Optical microscopy allows for imaging the phase separation in the V_2O_3 thin-film, because the metallic and insulating phases have different reflectivities (see Fig. 1(c)). Note that counterintuitively the insulating phase has a higher reflectivity than the metallic phase. The reason for this is that the monochromatic illumination at 528 nm is above the plasma frequency for both phases, and therefore the reflectivity contrast is not caused by the concentration of free charge carriers. Instead, e_g^π to a_{1g} (lower Hubbard band) [50, 51] interband transitions dominate the insulating-phase reflectivity, while transitions from the quasi-particle peak to the a_{1g} upper Hubbard band [48] dominate the metallic-phase reflectivity.

We measured the electric transport properties in a two-point configuration with a Keithley 2400 source/meter unit configured as current-source. IVCs were taken from 0 to 20 mA and back to 0 (between 0 and 3.5 mA the step size was 0.1 mA , then the step size was increased to 0.5 mA , and between 3.0 and 0 mA the step size was reduced to 0.1 mA).

III. THERMALLY DRIVEN MIT/IMT

A. Device Resistance

Figure 1(b), upper panel, shows the electrical resistance R vs. temperature T of the device, acquired with a bias current $I = 5\text{ }\mu\text{A}$. The large resistance change at the MIT by four orders of magnitude is indicative of

a high-quality V_2O_3 -thin-film with few defects. Due to the first-order nature of the MIT/IMT, the $R(T)$ -curve is hysteretic, with a MIT temperature T_{MIT} about 5 K below the IMT temperature T_{IMT} . Consequently, for the IVC measurements and imaging presented below, it has been vital to prepare a well-defined initial state in order to obtain reproducible results. This has been achieved by thermal cycling, i.e., by cooling or by heating to temperatures, where the V_2O_3 is in a pure insulating or metallic state, before heating or cooling to the targeted temperature.

B. Phase Separation at the MIT/IMT

We have acquired a temperature series of wide-field microscopy images during one thermal cycle with a 1 K stepsize across the MIT/IMT. Figure 1(c) shows a selection of images from this series. An extended photomicrograph series is included in appendix A 1 (Fig. 5). Capital letters indicate the corresponding temperatures in the $R(T)$ curve (Fig. 1(b) upper panel). By averaging over the area of interest, we obtain the temperature dependence of the reflectivity of the V_2O_3 film, normalized to the reflectivity of the Au electrodes (see Fig. 1(b), lower panel). The hysteresis in the $R(T)$ curve is well reproduced by the normalized reflectivity vs. T .

The photomicrographs acquired in the hysteretic temperature regime show spontaneous insulator/metal phase separation with herringbone-domains [43]. Domain patterns, bearing a strong resemblance to those observed here, can be found by numerical approximations to the Cahn-Larché equation, which describes the phase separation of a binary mixture in the presence of elastic stress (see Fig. 6 in [53]). A Fast Fourier Transform (FFT) analysis of the domain pattern is included in appendix A 2 (Fig. 6). The FFT analysis reveals that the domains have two preferred directions; one is at an angle $\alpha \approx 9^\circ$ at the MIT, which switches to $\alpha \approx 22^\circ$ at the IMT, and the second is at $\alpha \approx 79^\circ$, both at the MIT and IMT. α is the angle between the y -axis and the preferred direction (see coordinates in Fig. 1(c)). By comparing two optical images taken at the same temperature ($T = 168\text{ K}$) in the heating branch (IMT) for two consecutive thermal cycles (see Fig. 7 in appendix A 3), we find that the overall domain geometry (domain size and orientation) for repeated measurements is reproducible, as deduced from the FFT of the images. In real space, however, the domains may form in different locations in every heating cycle, despite a certain level of reproducibility. Interestingly, the heating and cooling cycles show significant differences in domain geometry. These results show that while there is some domain pinning, the local transition temperature depends strongly on cycle-dependent domain nucleation and growth which changes the local strain distribution. This indicates that the phase separation is not due to growth-induced local inhomogeneities (e.g. in chemical composition) of the thin-film, and that

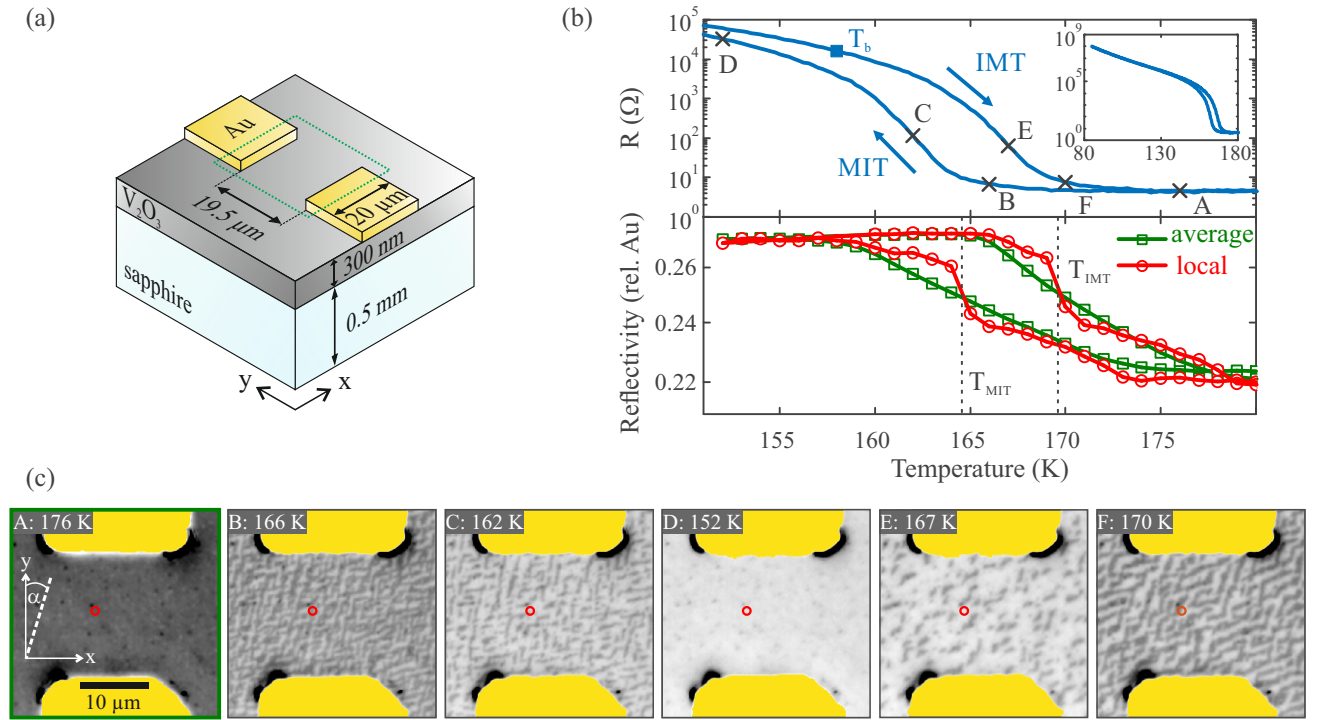


FIG. 1. (a) Schematic view of the planar V_2O_3 device under investigation. The two Au electrodes serve as combined current/voltage taps for two-probe electric transport measurements. The dotted green line indicates the area of interest (field of view of the images shown in (c)). (b) Resistively and optically detected MIT/IMT. UPPER PANEL: Electrical resistance $R(T)$ (measured with $I = 5 \mu\text{A}$); arrows indicate sweep direction of temperature T . Data points marked by letters correspond to images shown in (c). T_b indicates the base temperature set for the measurements presented in Fig. 3. INSET: $R(T)$ including the lowest temperature of the thermal cycle. LOWER PANEL: Reflectivity vs. T of the V_2O_3 film normalized to the reflectivity of the Au electrodes. The green curve represents the average over the area of interest, while the red curve represents the reflectivity of a single pixel at the location indicated by the red circles in (c). Vertical dashed lines indicate the local transition temperatures T_{MIT} and T_{IMT} , determined for the single pixel. (c) Selection of photomicrographs acquired during one thermal cycle. Au electrodes are indicated by yellow areas.

the domain configuration is plastic to a certain degree.

In Fig. 1(b), lower panel, we also include the reflectivity vs. T curve for a single pixel indicated by a red circle in the photomicrographs. The discontinuous steps in reflectivity at the MIT and IMT are indicative of a first-order phase transition [43].

C. Spatially Resolved Transition Temperatures

By analyzing the steps in reflectivity for every pixel of the photomicrograph temperature series, maps of the local MIT and IMT temperatures T_{MIT} and T_{IMT} , respectively, with a resolution of 1 K can be derived (see Fig. 2). The maps of T_{MIT} (Fig. 2(a)) and T_{IMT} (Fig. 2(b)) show different patches with different transition temperatures, whose shape and form resemble the herringbone domains in the photomicrographs. We note that the transition temperature maps shown in Fig. 2 constitute a single instance of the local IMT/MIT temperature variation, representing the strain-induced domain structure, but not an actual deterministic transition temperature map. These maps allow us in the numerical analysis (discussed be-

low) to consider how the strain-induced variation in local MIT/IMT temperatures affects the electrothermal breakdown.

IV. CURRENT-INDUCED IMT – RESISTIVE SWITCHING

In Fig. 3, we present electric transport data and simultaneously recorded photomicrographs for the current-induced IMT. We also include the results of numerical simulations for direct comparison. Note that we have added an animation to appendix C (Video 1) visualizing the resistive switching for every bias-point.

A. Current-Voltage Characteristics

Before the measurement, the device was brought into the heating branch (at the base temperature $T_b = 158$ K, cf. Fig. 1(b)) via thermal cycling. Then IVCs for two consecutive current sweeps were acquired (see Fig. 3(a)). During one sweep, the current increases from 0 mA to the

maximum value of 20 mA and decreases back to 0 mA. The arrows in Fig. 3(a) indicate the sweep direction. Starting at the origin of the graph, the IVCs progress almost linearly up to $I \approx 0.5$ mA, which indicates an almost Ohmic resistance. Upon further increasing I , the slope of the IVCs significantly increases, i.e., the differential resistance decreases. A section with negative differential resistance follows. A horizontal jump indicative of an instantaneous (within the measurement time scale) reduction of device resistance interrupts the IVCs at $I \approx 2.5$ mA. In other words, an electrical breakdown of the device causes resistive switching to a low-resistance state. After the jump, the IVCs progress almost vertically with further increasing I . When the current is reduced from its maximum value, the IVCs progress almost vertically down to $I \approx 1.8$ mA, which is below the value of the first horizontal jump. At this bias-point, there is a second horizontal jump indicative of an instantaneous increase of device resistance, i.e., the device switches back to a high-resistance state. A section with a decreasing slope and a linear section follows.

The IVCs of the first and second sweep are qualitatively similar. However, the maximum voltage, reached before the voltage jump appears in the upsweep, is reduced for the second sweep. For sweeps following the second sweep (not shown), the maximum voltage does

not change anymore and the IVCs are almost identical. Thermal cycling restores the IVC of the first sweep. We infer from the reproducibility of the IVC measurements that the observed resistive switching is non-destructive.

In addition to the very pronounced hysteresis in the low-bias-current regime where resistive switching occurs, we observe a small hysteresis in the high-bias regime, i.e., the downsweep branches have lower voltages than the upsweep branches (see inset Fig. 3(a)). Furthermore, in this high-bias regime, the IVCs show small saw-tooth like jumps (see inset Fig. 3(a)).

B. Imaging Filaments

Simultaneously with recording IVCs during a current sweep, photomicrographs were acquired. We present a selection of these photomicrographs in Fig. 3(b) (left column) for the second current sweep. The animation in appendix C (Video 1) shows a movie of the full current sweep.

The following remarks are crucial for interpreting the results: As deduced from the images acquired during temperature sweeps, metallic and insulating domains have different optical reflectivity, allowing us to assign metallic and insulating resistivities to dark and bright regions of the device, respectively. From Fig. 1(c), we learn that dark areas in the photomicrograph indicate a metallic V_2O_3 phase, while bright areas indicate an insulating phase.

Photomicrograph A in Fig. 3(b) was acquired at bias-point A on the upsweep branch of the second current sweep, just before the large voltage jump appears. The photomicrographs acquired between zero bias and bias-point A are all identical (see animation in appendix C, (Video 1)). The V_2O_3 thin-film between the electrodes is insulating (bright) with several small metallic (dark) inclusions, and the device is in a high-resistance state. The metallic inclusions appeared after the voltage jump of the first current sweep. Photomicrograph B corresponds to bias-point B immediately after the large voltage jump, indicating an abrupt switching of the device to a low-resistance state. A narrow metallic (dark) filament connects the electrodes at an oblique angle α , shunting the insulating film. With further increasing current, the filament width increases (see photomicrographs B–D) by growing to the right. bias-point D is at $I = 20$ mA, which terminates the upsweep branch. When the current is reduced, the filament splits into several branches (photomicrograph E). When the current is reduced further, the splitting results in multiple parallel filaments (photomicrograph F). Then these filaments disappear one after the other (photomicrographs F–H). Photomicrographs H and B are taken at almost the same current value and are almost identical. Finally, when the current is reduced to a bias-point just below the second voltage-jump, indicating an abrupt increase of the device resistance, the last remaining filament disappears, and the device returns to

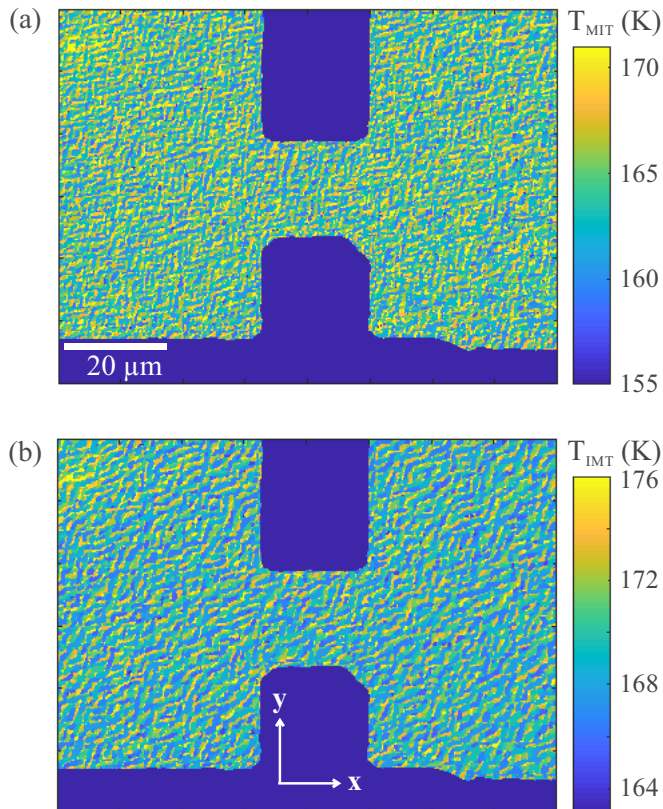


FIG. 2. Local transition temperatures of V_2O_3 thin-film device: (a) T_{MIT} map, (b) T_{IMT} map. Large dark blue areas indicate Au electrodes.

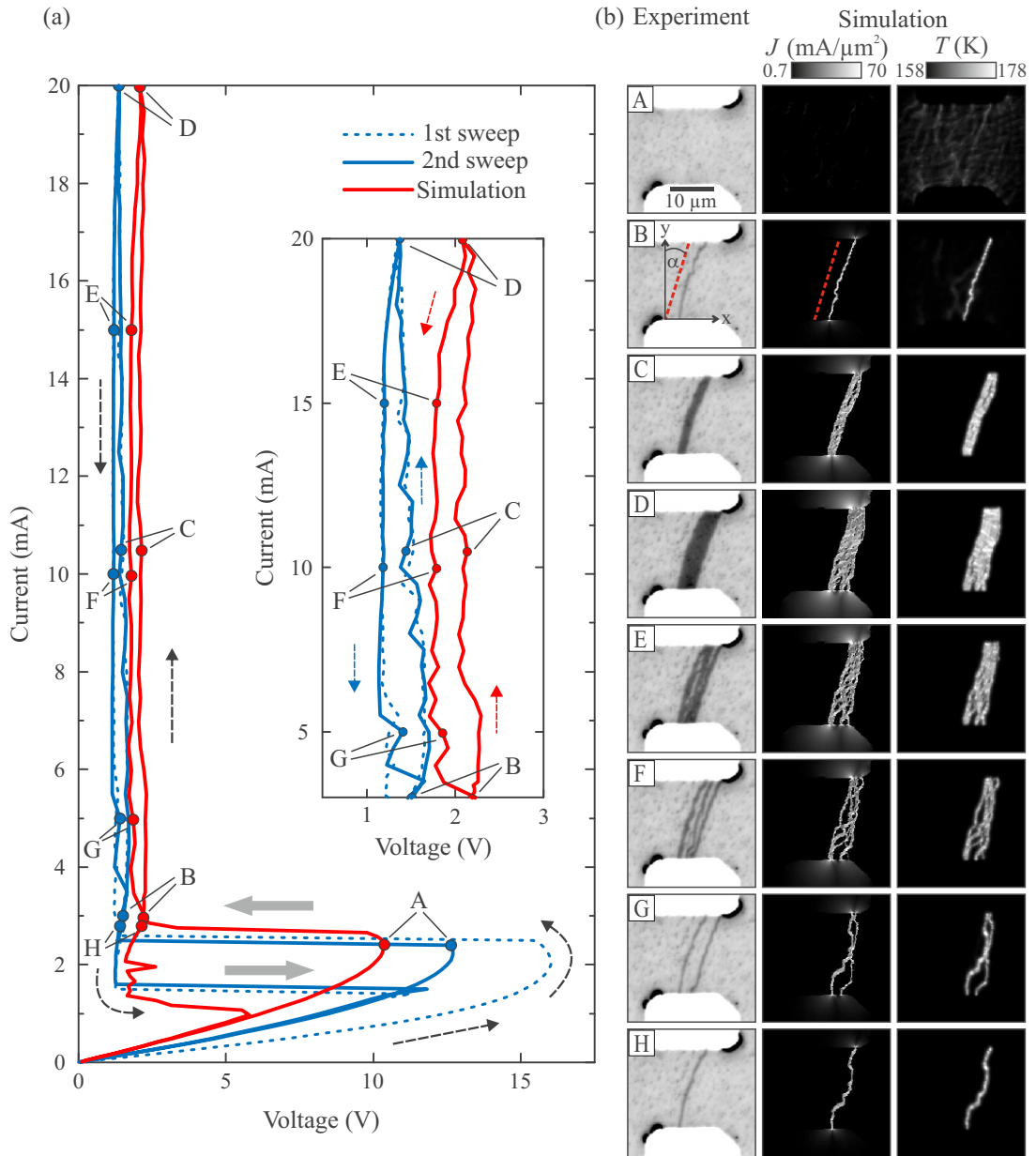


FIG. 3. Electrical breakdown in a planar V_2O_3 device at a base temperature $T_b = 158$ K at the onset of the IMT. (a) Measured (blue) and simulated (red) IVCs. Letters label data points for which images are shown in (b). The arrows indicate the sweep directions. The grey thick arrows indicate resistive switching to a low- and high-resistance state, respectively. INSET: Zoom on the high-current section. (b) LEFT COLUMN: Selection of photomicrographs acquired during the second current sweep. MIDDLE AND RIGHT COLUMN: Selection of the simulated spatial distribution of current density J and local device temperature T , respectively. The dashed red lines for images B indicate an $\alpha \approx 17^\circ$ inclination of the filament with respect to the y -direction.

an insulating, high-resistance state (see animation in appendix C, Video 1).

C. Discussion of Experimental Results

We derived additional relations (Fig. 4) from the IVC and photomicrographs of the second current sweep.

These relations help to interpret the results. The derivation of the conductance ($G = I/V$) vs. current and current vs. power ($P = I \cdot V$) relations (Fig. 4(a), (b), respectively) is straightforward. In Fig. 4(c), the filament width was estimated by dividing the dark filament area in the photomicrographs by the filament length, which was estimated by approximating the filament as a straight line. Similarly, the filament resistivity ρ_{filament} was de-

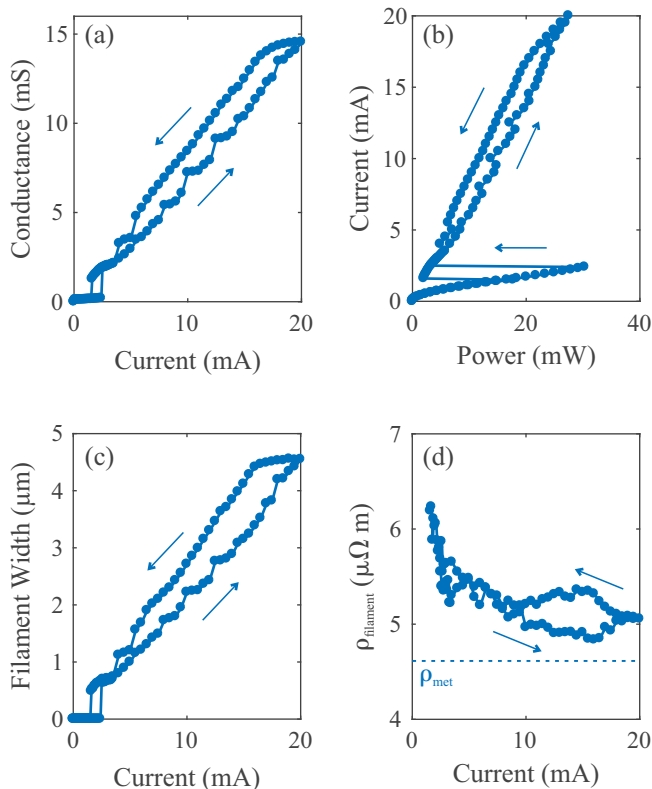


FIG. 4. Relations derived from the IVC and photomicrographs of the second current sweep in Fig. 3. (a) conductance vs. current, (b) current vs. power, (c) estimated total filament width vs. current, and (d) resistivity of the metallic phase estimated from filament width vs. current. The horizontal line indicates the resistivity of the metallic phase ρ_{met} used in the numerical simulations to obtain agreement with experimentally measured resistance in the metallic phase.

ried, assuming that the filament extends throughout the thickness of the V_2O_3 film.

Now, we revisit the IVCs and the photomicrographs shown in Fig. 3. The overall behavior of the device is characteristic of an electrothermal breakdown [37]. The increasing slope, after the linear (Ohmic) section in the low-bias-current regime before switching to the high-resistance state, can be explained by a decrease of the device resistance due to Joule heating. According to the $R(T)$ curve shown in Fig. 1(b), close to the IMT an increase in device temperature results in a considerable decrease in device resistance. This effect produces the observed back-bending of the IVC. The system then becomes electrothermally unstable, and the horizontal jump is the result of the formation of an electrothermal filament. Figure 3(b) image B clearly shows the appearance of this metallic filament. The vertical progression of the IVC with increasing I after switching to the low-resistance state is associated with an increase in filament width (see Fig. 3(b) images B–D). The second horizontal

jump during the return current sweep indicates an abrupt increase of the device resistance associated with the disappearance of the conducting filament (see animation in appendix C, Video 1).

From Fig. 4(b), we learn that resistive switching occurs at maximum power. Considering the IVC of the 2nd sweep (Fig. 3(a)), there is a slight back-bending before the jump indicating resistive switching. In the IVC of the 1st sweep, this back-bending is more pronounced. If resistive switching were purely electric-driven, the resistive switching would occur at maximum voltage, which is not the case. This is further evidence for an electrothermal breakdown. According to Fig. 4, in the high-bias regime after resistive switching, the device conductance, power, and filament width have an overall linear current dependence, while the filament resistivity is almost constant. Again, these dependencies are characteristic of an electrothermal breakdown, where the device current flows in a metallic filament, and the current controls the width of this filament via Joule heating. Fig. 4(d) shows good agreement of the filament resistivity with the resistivity of the metallic phase ρ_{met} used for numerical simulations (see section “D. Numerical model” below). We note that the initial step decrease of ρ_{filament} vs. I in Fig. 4(d) might be due to the possibility that right after its formation (or before its extinction), the filament does not yet expand throughout the entire film thickness and/or that the filament width is below the spatial resolution of the microscope. In both cases, we would slightly overestimate ρ_{filament} . However, we also note that the independently determined conductance vs. current (Fig. 4(a); from IVCs) and filament width vs. current (Fig. 4(c); from images) curves match very closely, including the jumps at distinct current values. This indicates that the minimum filament width is very likely not much smaller than what we observe by imaging. Moreover, this again clearly demonstrates how the overall device resistance in the low-resistance state is governed by the optically detected filamentary structures.

We observe atypical effects, which can only be explained by features that are not included in the most simple electrothermal model. First, the filament is not straight along the y -axis, but rather connects the electrodes at an oblique angle α of approximately 17° with respect to the y -direction (see image B in Fig. 3(b)). In a homogeneous medium, one would expect that the shortest possible current path is preferred, and the filament should follow the y -direction. Second, during the down-sweep the filament first splits into several branches, and then it divides into multiple parallel filaments (see images E and F in Fig. 3(b)). Because adjacent regions in the film are thermally coupled in the lateral direction, for a homogeneous medium one would expect that, as current decreases, the filament shrinks from its sides, since the filament temperature is highest in its center, so that the colder sides would transition into the insulating state more readily. Third, for high bias currents in the low-resistance state, there is hysteresis in the IVC (see

inset Fig. 3(a)) and in the conductance, power and filament width vs. current relations (Fig. 4). However, after an electrothermal breakdown in a homogeneous medium without thermal hysteresis, the current should control these parameters without hysteresis in the IVC.

D. Numerical model

We developed a numerical model to investigate whether the electrical breakdown is electrothermal and whether the phenomena which are atypical for an electrothermal breakdown in a homogeneous medium without thermal hysteresis result from the strain-induced spatial variation of the MIT/IMT temperatures (see Fig. 2). A detailed description, based on Ref. 54, is given in appendix B.

The numerical model is based on a two-dimensional resistor network (see appendix B 1, Fig. 8), for which the current distribution is solved via mesh current analysis, while the thermal properties are modeled with a finite difference approximation of the time-dependent heat equation. The heat conduction was incorporated using the backward Euler method. Latent heat was included. We accounted for the thermal coupling to the cryostat cold-plate.

The four (or three) resistors of every cell in the 2D network have an individual hysteretic $R(T)$ dependence with MIT/IMT-temperatures corresponding to the experimentally determined values of Fig. 2. Deep in the insulating state, we assume the same resistivity $\rho_{\text{ins}}(T)$ for all cells which is determined from the measured $R(T)$ curve, and in the metallic state, we assume a constant $\rho_{\text{met}} = 4.6 \mu\Omega\text{m}$ for all cells, also determined from the measured $R(T)$ curve (Fig. 1(b)). With this approach, the strain-induced variation of the MIT/IMT-temperatures is included in the model. For a detailed description see appendix B 2.

Prior to the simulation of an entire current-sweep sequence, for each pixel the high- or low-resistance state within the hysteretic T -range is set, depending on history. This procedure takes into account, e.g., previous current-sweep sequences and hence can capture history effects in simulations for different current sweeps. For a given bias current value, the mesh current analysis and the time-dependent heat equation is solved with small time steps until the solution reaches a steady state. Subsequently, the procedure is repeated with an incremented current value. This way, we calculate the IVC and the spatial distribution of the current density J and the temperature T .

E. Comparison of Simulations with Experimental Results

The simulation results are included in Fig. 3 for direct comparison with the experimental data. The model

was numerically stable over almost the whole parameter space, except for a section in the first current sweep after the resistive switching. For this reason, we focus our discussion on the second sweep. We note that the simulation of the first sweep reveals that after return to zero current, some resistors remain in the metallic state. This is consistent with the imaging results, which show that metallic inclusions appear after the first sweep. For the simulation of the second sweep, this information from the simulation of the first sweep has been included, which explains why we find different results also in the simulations of different sweeps.

The heuristic numerical model, which includes strain-effects in the V_2O_3 thin-film indirectly via the IMT/MIT temperature maps, reproduces the resistive switching very well. Comparing the simulated IVC with the measured IVC in Fig. 3(a), the threshold currents for resistive switching are very similar, and the maximum voltage in the simulation is only 14% smaller than in the experiment. The model reproduces the appearance and disappearance of the metallic filament accompanying resistive switching (see Fig. 3(b) and animation in appendix C, Video 1). Additionally, the effects, which are atypical for an electrothermal breakdown (discussed above), are reproduced as well.

The agreement of the electrothermal model with the experimental results supports the hypothesis that an electrothermal breakdown induces resistive switching. Simulated images for bias-points A and B in Fig. 3(b) demonstrate the current- and temperature redistribution. As discussed in the introduction, this redistribution results from a runaway effect driven by electrothermal instability. In particular, the simulation for bias-point A shows already an inhomogeneous T distribution within the entire device area prior to resistive switching. After switching to the low-resistance state at bias-point B, a single metallic filament appears in the optical image, and the simulation shows that the current density is concentrated in this filament, with a local temperature of $\sim 20\text{K}$ above the base temperature T_b , while the area outside the filament has cooled down. In bias-point B, the simulation still shows a few filamentary regions with slightly enhanced temperature, while with further sweeping up the bias current, these areas also cooled down close to T_b .

Remarkably, the simulated data do not only reproduce all the experimentally observed features in the IVCs, but also in the shape and direction of the metallic filament. The filaments in the photomicrographs and the simulation both connect the electrodes at an oblique angle of $\alpha \approx 17^\circ$, following roughly one preferred axis of the herringbone domains (see Fig. 1(c)). The minimum filament width, right before the device switches back to the high-resistance state, is approximately $0.5 \mu\text{m}$, which corresponds to the domain size. However, we note that the value of $0.5 \mu\text{m}$ has to be considered as an upper limit, as this is also the spatial resolution of the optical microscope. These observations support the idea that the

herringbone domain structure significantly affects the details of resistive switching.

The effects atypical of an electrothermal breakdown, like hysteresis and sawtooth-like jumps in the IVC, filament branching and splitting seem to have the same cause: a hysteretic and strain-induced heterogeneous electrothermal medium.

Considering the overall shape of the IVCs shown in Fig. 3, the voltage is almost constant in the low-resistance state. This behavior is typical for an electrothermal breakdown, where a Joule heating filament controls the voltage across the device. Usually, the filament growth with applied current is reversible, and the increasing and decreasing current curves are congruent in this bias regime. However, the IVCs are hysteretic (see inset in Fig. 3(a)). We argue that the hysteresis in the thermally driven MIT/IMT, i.e., the shift between the MIT- and IMT-temperatures in V_2O_3 , is causing this hysteresis in the IVCs. When the device is biased on the increasing current branch, the width of the filament increases, and more and more regions undergo an IMT. For electrical bias on the decreasing current branch, the situation reverses, i.e., the width of the filament reduces, and more and more regions undergo a MIT. As $T_{IMT} > T_{MIT}$, more Joule heating power is required to drive regions through the IMT on the increasing current branch than on the decreasing current branch, when regions are driven through the MIT. Hence, for a given current I , the voltage V is higher in the increasing current branch than in the decreasing current branch.

The sawtooth-like IVC jumps (inset in Fig. 3(a)) are due to discontinuous generation and extinction of entire filaments or segments of filaments. We attribute this to filament edge pinning of boundaries between the insulating and metallic phase due to the spatial variation in local MIT/IMT-temperatures. In particular, the filament does not grow continuously as the current is increased but switches adjacent domains to the metallic state as soon as the dissipated power is sufficient. For increasing currents, only a single filament is visible in the photomicrographs, whose width increases for increasing currents. For decreasing currents, the expected behaviour would be that the filament width decreases continuously. However, the filament branches and splits into multiple filaments (see Fig. 3 and the animation in appendix C, Video 1). The varying local MIT/IMT-temperatures (see Fig. 2) define percolation paths to which the filaments can lock in. Consequently, when the current is reduced, it distributes along these percolation paths. The geometry of these paths closely resembles the spontaneously forming domain configuration observed during temperature sweeps in the phase coexistence regime at the MIT. For the same reason, the filament is not connecting the electrodes along the shortest path but at an oblique angle. In contrast to the filament in the photomicrographs, the filament in the simulation consists of multiple filaments for biasing on the increasing current branch, although it is more compact than for the decreasing current branch.

One explanation is that we cannot resolve these multiple filaments in the photomicrographs due to the limited resolution of the microscope. Another explanation is that the simulation uses transition temperature maps derived from a series of fixed domain patterns, while in reality the domains are plastic (see discussion in Sec. IIIB and Fig. 7 in appendix A 3), i.e., domain walls can move. Due to this plasticity, there might be a tendency of the domains to merge, which is not reflected in the numerical model.

V. CONCLUSIONS

We demonstrated electrothermally induced resistive switching in a current-biased planar V_2O_3 thin-film device with a base temperature at the onset of the IMT. Photomicrographs show the appearance of a metallic filament that accompanies resistive switching. A model of the resistive switching reveals that the spatial variation in local MIT/IMT-temperatures influences the details of the electrothermal breakdown.

The variation of local MIT/IMT temperatures is the result of strain minimization in the V_2O_3 thin-film, and we conclude that elastic energy influences resistive switching properties by affecting the filament configuration. Therefore, the influence of strain on the dynamics of switching devices should be taken into account and may allow for novel ways of tuning their properties.

These findings demonstrate the crucial role played by Joule heating and strain-effects in this class of memristive devices, which are considered as promising building blocks in neuromorphic computing. Obviously, the approach taken in this work can also be applied to other Mott insulator systems.

ACKNOWLEDGMENTS

This work was supported as part of the Quantum Materials for Energy Efficient Neuromorphic Computing (Q-MEEN-C) Energy Frontier Research Center (EFRC), funded by the U.S. Department of Energy, Office of Science, Basic Energy Sciences under Award # DE-SC0019273. Part of the fabrication process was done at the San Diego Nanotechnology Infrastructure (SDNI) of UCSD, a member of the National Nanotechnology Coordinated Infrastructure (NNCI), which is supported by the National Science Foundation under grant ECCS-1542148. Yoav Kalcheim acknowledges the support of a Norman Seiden Fellowship in Nanotechnology and Optoelectronics.

M. L. and S. G. contributed equally to this work.

Appendix A: Phase Separation at the MIT/IMT

This section provides further details on the phase separation of the investigated V_2O_3 film across the metal-to-insulator transition (MIT) and the insulator-to-metal transition (IMT).

1. Evolution of domain configurations across the MIT/IMT

Figure 5(b) shows a more detailed series of photomicrographs at temperatures T across the MIT/IMT. The resistance R vs T curves (Fig. 5 (a)) were acquired with a bias current $I = 5 \mu\text{A}$. The capital letters indicate the acquisition temperatures of the photomicrograph series.

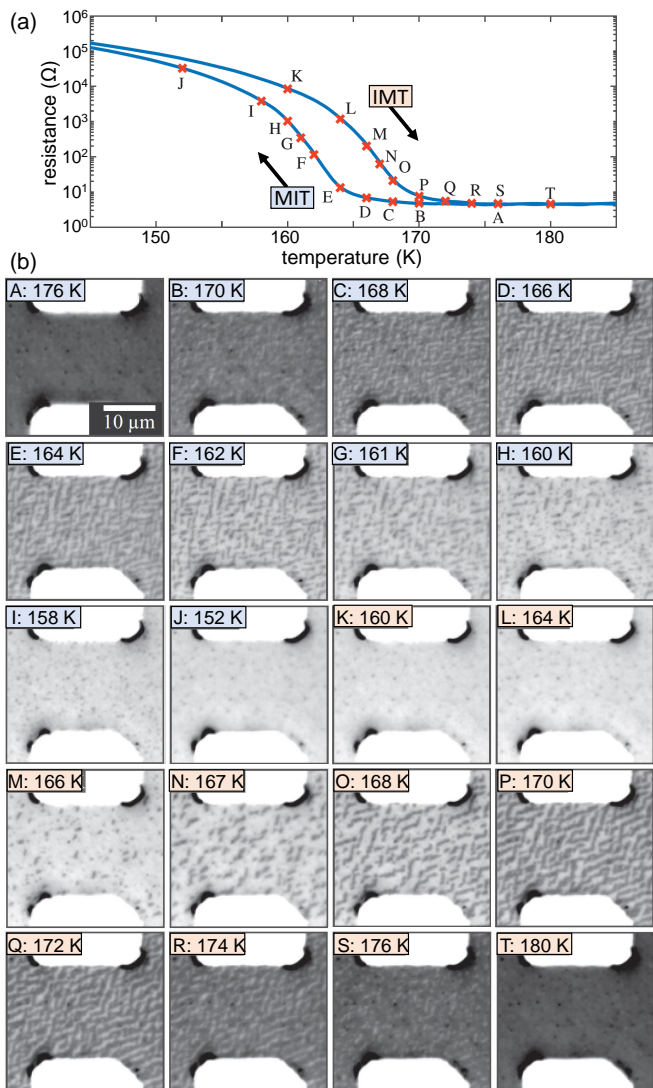


FIG. 5. Phase separation in V_2O_3 at the MIT/IMT: (a) $R(T)$ curves. (b) Images acquired at the points, labeled A to T in (a), during cool-down and warm-up of the sample.

The $R(T)$ curves show a four-order of magnitude change of R across the MIT/IMT, with a thermal hysteresis of ≈ 5 K between cooling and heating branches. The minimum temperature within the thermal cycle was 80 K.

The transition between the two phases progresses through the formation of domain patterns with dark and bright contrast that are identified as metallic and insulating regions, respectively. Starting from a homogeneous metallic state (A: 176 K), small insulating islands begin to form (B: 170 K) that grow and connect to form a herringbone-like domain pattern (C: 168 K and D: 166 K). At this point, the metallic domains still provide continuous paths connecting the electrodes. These get disconnected when the temperature is further decreased (E: 164 K and F: 162 K), which goes along with a step increase in resistance, as the current now has to flow through parts of the film that are in the insulating phase. At even lower temperatures (G: 161 K, H: 160 K, and I: 158 K) the V_2O_3 film is in a state where metallic patches are embedded within an insulating matrix. The size of the metallic domains decreases with decreasing temperature until the sample is in an almost homogeneous insulating state (J: 152 K).

The heating branch shows a slightly different behavior. Beginning from the insulating state (K: 160 K), small metallic islands appear (L: 164 K and M: 166 K) that connect to elongated domains (N: 167 K and O: 168 K). These domains are wider than the domains in the cooling branch and have a different preferred direction. Upon further increase of the temperature, more metallic domains appear and long metallic paths are created that eventually form continuous metallic paths that connect the electrodes (P: 170 K). The metallic regions grow (Q: 172 K and R: 174 K) until only isolated insulating patches are left (S: 176 K). Eventually the film arrives in a homogeneous metallic state (T: 180 K).

2. Directionality and periodicity of the domain patterns

The preferred direction of the domains and their periodicity can be estimated from the fast Fourier transform (FFT) of the optical images. This is shown for selected temperatures in Fig. 6. Angles are measured clockwise with respect to the vertical axis, i.e., those correspond to the definition of α for optical images in the manuscript. The FFT of the domain configuration in the MIT [Fig. 6 (a) and (b)] clearly shows four peaks that correspond to directions of $\approx 99^\circ$ and $\approx 169^\circ$, with a mean periodicity of $\approx 1.3 \mu\text{m}$ at 166 K and $\approx 1.5 \mu\text{m}$ at 162 K. The preferred orientations of the long axis of the domains in real space are perpendicular to the directions found in the FFT and are indicated by the broken lines at $\approx 9^\circ$ and $\approx 79^\circ$ in the optical images. Figure 6 (c) and (d) show the domain configuration and FFT for temperatures of 168 K and 172 K in the IMT. At $T = 168$ K, it is not possible to distinguish the peaks

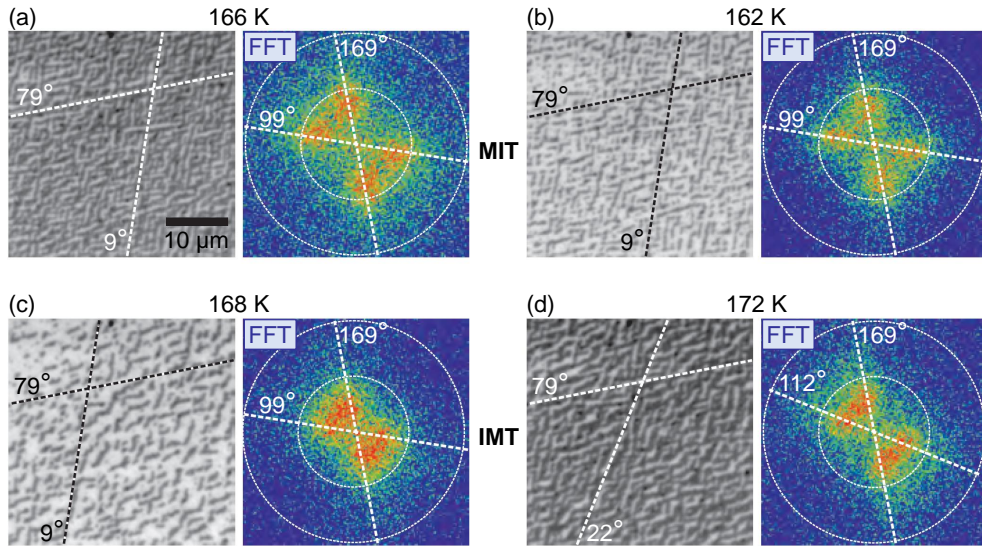


FIG. 6. Domain configuration (left) and fast Fourier transform (right) for selected temperatures of (a) 166 K and (b) 162 K in the cooling branch (MIT) and (c) 168 K and (d) 172 K in the heating branch (IMT). The dashed lines highlight the predominant directionality of the long axis of domains in the real-space images and the directions at which the peaks occur in the FFT. The angles are measured clockwise with respect to the vertical axis. The inner (outer) circles in the FFT correspond to a spatial frequency of $1/\mu\text{m}$ ($2/\mu\text{m}$).

of the 99° and 169° -axes in the FFT. However, the real space image at 168 K shows that many of the domains still are oriented along the 9° and 79° -axes, while some domains have an orientation that lies in between these axes. At 172 K, on the other hand, only few domains are oriented along the 9° -axis, and the preferred directions become 22° and 79° , which is observed in the FFT as a narrowing of the peaks in angular direction. The mean periodicity of the domains in the heating branch (IMT) is found to be $\approx 2.2 \mu\text{m}$ at 168 K and $\approx 1.8 \mu\text{m}$ at 172 K.

3. Reproducibility of the domain configuration

Figure 7 (a) and (b) show the domain configuration at 168 K in the heating branch for two subsequent measurement runs. A complete thermal cycle (heating to room temperature and cooling to 80 K) separates the two images. While the overall density of metallic domains is similar, the domain patterns differ significantly. For comparison, a color-coded superposition of the images in Fig. 7 (a),(b) is shown in Fig. 7 (c). Metallic domains that are present in both, Fig. 7 (a) and (b), appear dark. Domains that are present only in image (a) are represented in green, those that are only present in (b) in red. It is apparent, that the domain configuration for repeated measurements is neither deterministic nor random. The same holds true for other temperatures in both the MIT and IMT. This indicates that the phase separation is not due to growth-induced local inhomogeneities of the film, for example in chemical composition, that could lead to a spatially varying transition temperature but rather is

caused through minimization of local strain as proposed by McLeod *et al.* [43].

Appendix B: Numerical Model

This section describes the numerical model, which has been used to simulate the current-voltage characteristics (IVCs) and spatial distribution of temperature T and current density J in the V_2O_3 films. This description is based on chapter 5.4 in Ref. 54.

1. Resistor network and mesh current analysis

To calculate the current distribution the sample is approximated by a 2-dimensional resistor network that is constructed from a square primitive cell with edge length $\Delta x = \Delta y$ that contains one node and four resistors. The resulting resistor network, obtained by assembling n primitive cells in x -direction and m primitive cells in y -direction, is shown in Fig. 8. The four resistors within each primitive cell with index i, j with $i \in \{1, m\}$ and $j \in \{1, n\}$ are assigned the same resistance $R_{i,j}$. The resistors at the left and right edge of the resistor network are truncated, making the boundary insulating, and a perfectly conducting wire connects the bottom and top edge to the current source. The loops formed by four neighbouring nodes and the resistors between them are called essential meshes.

For the complete resistor network one obtains a set of $a = (n - 1)(m + 1)$ equations for a essential meshes plus

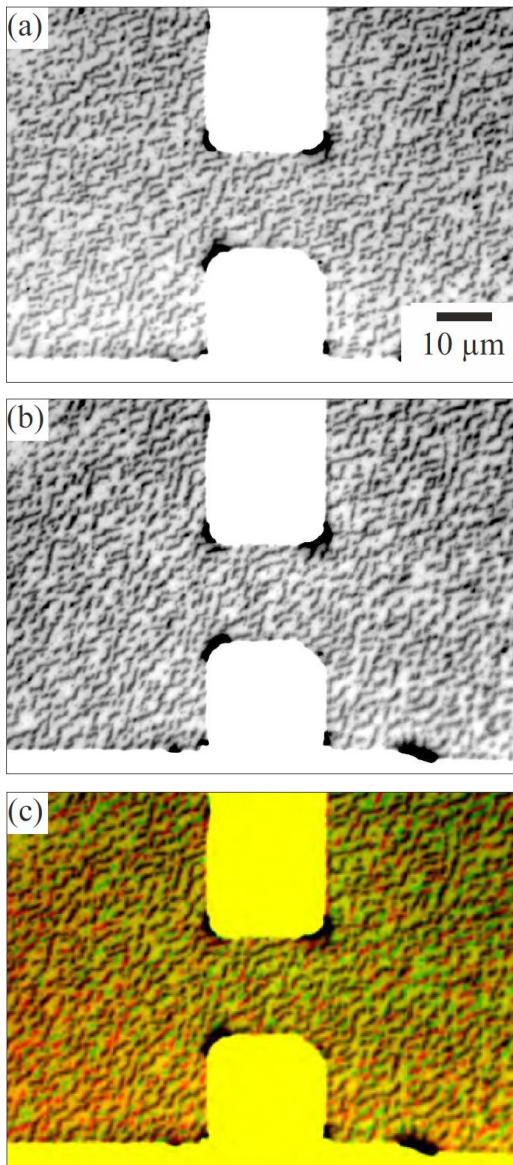


FIG. 7. Reproducibility of domain configuration. (a), (b) Optical images, recorded at 168 K in the heating branch for two subsequent runs with a full thermal cycle in between. (c) Color-coded superposition of images from (a) and (b). Metallic domains that are present in both (a) and (b) appear dark. Metallic domains only present in (a) are green, and only present in (b) are red. Insulating domains present in both micrographs are shown in yellow.

the equation for the current source mesh, which serves as a boundary condition. This set of equations is assembled into a $(a + 1) \times (a + 1)$ matrix \mathbf{EC} so that the equation system can be written in matrix form as

$$\mathbf{EC} \cdot \begin{pmatrix} I_{11} \\ \vdots \\ I_{1,n-1} \\ \vdots \\ I_{m+1,n-1} \\ I \end{pmatrix} = \begin{pmatrix} 0 \\ \vdots \\ 0 \\ \vdots \\ 0 \\ V \end{pmatrix}. \quad (\text{B1})$$

Solving this equation system returns for a given bias current I the voltage V across the network and the mesh currents, from which the current through each of the four resistors in the primitive cell i, j can be calculated according to

$$\begin{aligned} I_{i,j,1} &= I_{k,l} - I_{k,l-1} \\ I_{i,j,2} &= I_{k+1,l} - I_{k,l} \\ I_{i,j,3} &= I_{k+1,l} - I_{k+1,l-1} \\ I_{i,j,4} &= I_{k+1,l-1} - I_{k,l-1}, \end{aligned} \quad (\text{B2})$$

where, by convention, currents flowing in positive x - and y -direction have positive sign. These describe the current flow between adjacent primitive cells and are defined on the boundary between them (cf. Fig. 9).

Although it is not properly defined, it is desirable to evaluate the current density at the nodes. This is calculated by interpolating the current densities at the boundaries of the primitive cell, which delivers the current densities $J_{i,j}^x$ in x -direction and $J_{i,j}^y$ in y -direction, as well as

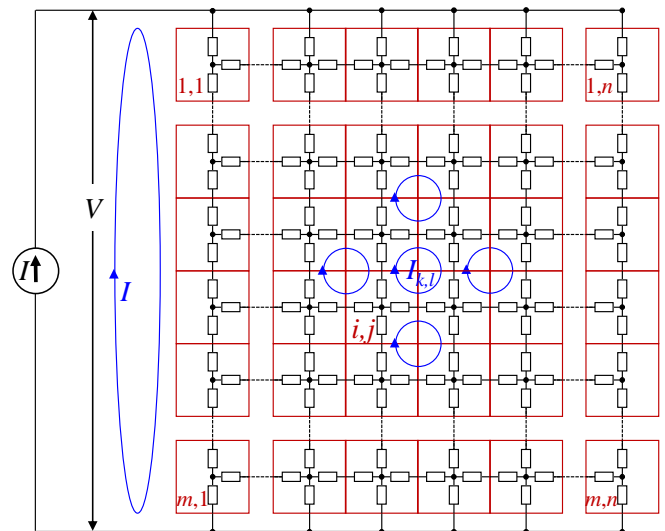


FIG. 8. Resistor network of $m \times n$ primitive cells used to approximate the resistance of the sample. Each primitive cell (red squares) contains one node and four resistors (except for the columns $j = 1$ and $j = n$ with only three resistors per primitive cell). A mesh current $I_{k,l}$ (blue) flows in each of the essential meshes of the resistor network. An additional mesh containing the current source is connected to the left side of the resistor network.

the magnitude of the current density $J_{i,j}^{\text{norm}}$

$$\begin{aligned} J_{i,j}^x &= \frac{I_{i,j,2} + I_{i,j,4}}{2 \Delta y d_f} \\ J_{i,j}^y &= \frac{I_{i,j,1} + I_{i,j,3}}{2 \Delta x d_f} \\ J_{i,j}^{\text{norm}} &= \sqrt{(J_{i,j}^x)^2 + (J_{i,j}^y)^2}, \end{aligned} \quad (\text{B3})$$

with the film thickness d_f . Note that these quantities approach the correct value only for $\Delta x, \Delta y \rightarrow 0$ and might deviate from the correct solution for finite dimensions of the primitive cell. Therefore, they are only used for displaying the results and not as input for further calculations. The power density $p_{i,j}$ generated through Joule heating in the primitive cell of volume $V_{i,j}$ is a quantity that will be used for modeling the thermal characteristics of the sample and is given by

$$p_{i,j} = \frac{P_{i,j}}{V_{i,j}} = \frac{R_{ij}}{\Delta x \Delta y d_f} (I_{i,j,1}^2 + I_{i,j,2}^2 + I_{i,j,3}^2 + I_{i,j,4}^2). \quad (\text{B4})$$

For the reasons mentioned above, the currents through the boundaries are used to calculate the power dissipated in the resistors within the primitive cell.

2. Definition of temperature-dependent resistivity

To approximate the temperature dependence of the resistivity of the V_2O_3 film, the following assumptions are made: (i) The resistivity ρ_{met} in the metallic phase is constant with respect to temperature and lateral position. (ii) The resistivity ρ_{ins} deep in the insulating phase (at temperatures far below the MIT/IMT temperatures) is homogeneous and has the same temperature dependence as the globally measured $R(T)$. (iii) For cool-down of the sample, the increase in resistivity from ρ_{met} to ρ_{ins} in the transition region is described by a function $f(T_{\text{MIT}}(x,y) - T)$ that increases from 0 above the MIT

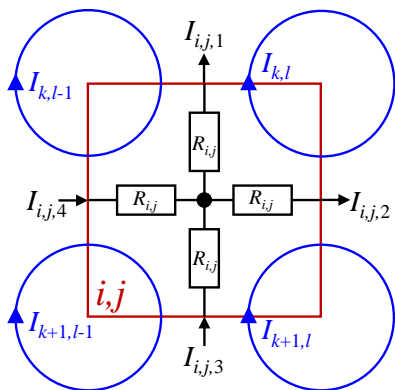


FIG. 9. On the definition of the currents $I_{i,j,1}$ to $I_{i,j,4}$ flowing through the resistors in the primitive cell i,j , which are calculated from the adjacent mesh currents.

temperature T_{MIT} to 1 at low temperatures. Accordingly, the local resistivity for cool-down of the sample is described by the function

$$\rho_{\text{MIT}}(x,y,T) = \rho_{\text{ins}}(T) f(T_{\text{MIT}}(x,y) - T) + \rho_{\text{met}}. \quad (\text{B5})$$

(iv) Similarly, for warm-up of the sample, the decrease in resistivity in the transition region is described by the same function $f(T_{\text{IMT}}(x,y) - T)$, that now has the difference between the IMT temperature T_{IMT} and the temperature as argument

$$\rho_{\text{IMT}}(x,y,T) = \rho_{\text{ins}}(T) f(T_{\text{IMT}}(x,y) - T) + \rho_{\text{met}}. \quad (\text{B6})$$

Since the transition temperatures vary spatially, this leads to an inhomogeneous distribution of the resistivity in the transition region, while the resistivity is homogeneous outside the transition region. Note that the transition temperatures $T_{\text{MIT}}(x,y)$ and $T_{\text{IMT}}(x,y)$ that are used here to define the temperature dependence of the resistivity have been determined experimentally (cf. Fig. 2), which should allow for a good representation of the spatial dependence of the resistivity.

The resistivity in the metallic phase has been derived from experimental data as $\rho_{\text{met}} = 4.618 \times 10^{-6} \Omega\text{m}$. The resistivity at low temperatures was obtained by fitting the measured $R(T)$ curve in the temperature range from 80 K to 130 K with the function

$$\rho_{\text{ins}}(T) = ae^{bT} + ce^{dT}, \quad (\text{B7})$$

with $a = 4.66 \times 10^8 \Omega\text{m}$, $b = -0.1926/\text{K}$, $c = 3.19 \times 10^5 \Omega\text{m}$, and $d = -0.09849/\text{K}$. The function f that describes the transition between the metallic and insulating phase is obtained by running the mesh current analysis with the matrix $R_{i,j}(T)$ as input for temperatures throughout the transition region and adjusting f until the measured resistance is reproduced. The resulting temperature-dependent resistivity is shown in Fig. 10.

3. Finite-difference approximation to heat equation

Heat transfer in solids is described by the parabolic partial differential equation, known as the heat equation,

$$\rho c_P \frac{\partial T}{\partial t} - \nabla \cdot (k \nabla T) = \dot{q}_V, \quad (\text{B8})$$

with the density ρ , the heat capacity at constant pressure c_P , the thermal conductivity k , and the volumetric heat source \dot{q}_V . In two dimensions and for a film thickness d_f this can be written as

$$\rho c_P \frac{\partial T}{\partial t} - \frac{\partial}{\partial x} \left(k_x \frac{\partial T}{\partial x} \right) - \frac{\partial}{\partial y} \left(k_y \frac{\partial T}{\partial y} \right) = \dot{q}_V, \quad (\text{B9})$$

or, if the thermal conductivity $k = k_x = k_y$ is isotropic, as

$$\frac{\partial T}{\partial t} - \kappa \left(\frac{\partial^2 T}{\partial x^2} + \frac{\partial^2 T}{\partial y^2} \right) = \frac{\dot{q}_V}{\rho c_P}, \quad (\text{B10})$$

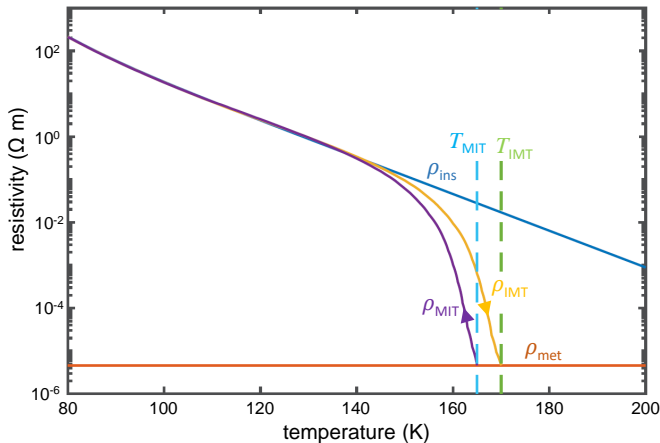


FIG. 10. Modeling of the temperature dependence of the V_2O_3 resistivity. For the cooling branch ρ_{MIT} increases from ρ_{met} to ρ_{ins} for $T < T_{MIT}$ (blue dashed line). In the heating branch ρ_{IMT} decreases towards T_{IMT} (green dashed line).

with the thermal diffusivity $\kappa = k/(\rho c_P)$. The partial derivatives in the heat equation can be approximated by finite differences. The same discretization in space as for the mesh current analysis will be used and the variables are evaluated on the central node of the primitive cell with index i, j . The time is discretized into time steps Δt and an index τ is introduced describing the point in time. The heat equation can be approximated in space and time using a number of finite-difference methods. Here, the backward Euler method is used which, in con-

trast to the forward Euler or Crank-Nicolson method, is unconditionally stable and immune to oscillations. For a node spacing of Δx and Δy and a time step Δt the implicit discrete form of Eq. (B10) is given by

$$\frac{T_{i,j}^{\tau+1} - T_{i,j}^{\tau}}{\Delta t} - \kappa \left(\frac{T_{i,j+1}^{\tau+1} - 2T_{i,j}^{\tau+1} + T_{i,j-1}^{\tau+1}}{(\Delta x)^2} + \frac{T_{i+1,j}^{\tau+1} - 2T_{i,j}^{\tau+1} + T_{i-1,j}^{\tau+1}}{(\Delta y)^2} \right) = \frac{\dot{q}_{i,j}^{\tau}}{\rho c_P}. \quad (\text{B11})$$

At this point, an additional thermal coupling to the bath with temperature T_b is introduced which is a consequence of the heat flow to the coldfinger through the substrate of thickness d_s and an effective thermal conductivity k_s . This can be modeled as a heat source $\dot{Q}_b = k_s (T_b - T_{i,j}^{\tau+1}) \Delta x \Delta y / d_s$ that is given by the power that is transferred to the bath through a cuboid with cross section $\Delta x \Delta y$ and length d_s . Accordingly, the volumetric heat source in Eq. (B11) is represented by the sum of Joule heating $p_{i,j}$ and a contribution of \dot{Q}_b lumped to the volume $V_{i,j}$

$$\dot{q}_{i,j}^{\tau} = p_{i,j}^{\tau} + \frac{\dot{Q}_b}{V_{i,j}} = p_{i,j}^{\tau} + \frac{k_s}{d_f d_s} (T_b - T_{i,j}^{\tau+1}). \quad (\text{B12})$$

It is further assumed, that the node spacing in x - and y -direction is equal ($\Delta x = \Delta y$). With the thermal diffusivity to the bath $\kappa_s = k_s/(\rho_s c_{P,s})$, Eq. (B11) becomes

$$T_{i,j}^{\tau+1} - T_{i,j}^{\tau} - \frac{\kappa \Delta t}{(\Delta x)^2} (T_{i-1,j}^{\tau+1} + T_{i,j-1}^{\tau+1} - 4T_{i,j}^{\tau+1} + T_{i,j+1}^{\tau+1} + T_{i+1,j}^{\tau+1}) = \frac{p_{i,j}^{\tau} \Delta t}{\rho c_P} + \frac{\kappa_s \Delta t}{d_f d_s} (T_b - T_{i,j}^{\tau+1}). \quad (\text{B13})$$

Rearranging this equation so that terms at time $\tau + 1$ are on the left hand side and terms at time τ are on the right hand side, and introducing the coefficients $A_f = \kappa \Delta t / (\Delta x)^2$, $A_b = \kappa_s \Delta t / (d_f d_s)$, and $A_q = \Delta t / (\rho c_P)$, results in

$$-A_f T_{i-1,j}^{\tau+1} - A_f T_{i,j-1}^{\tau+1} + (1 + 4A_f + A_b) T_{i,j}^{\tau+1} - A_f T_{i,j+1}^{\tau+1} - A_f T_{i+1,j}^{\tau+1} - A_b T_b = T_{i,j}^{\tau} + A_q p_{i,j}^{\tau}. \quad (\text{B14})$$

These equations are assembled into a $(m \cdot n + 1) \times (m \cdot n + 1)$ heat transfer matrix \mathbf{HT} so that the equation system is given by

$$\mathbf{HT} \cdot \begin{pmatrix} T_{11}^{\tau+1} \\ \vdots \\ T_{1n}^{\tau+1} \\ \vdots \\ T_{m,n}^{\tau+1} \\ T_b \end{pmatrix} = \begin{pmatrix} T_{11}^{\tau} + A_q p_{1,1}^{\tau} \\ \vdots \\ T_{1n}^{\tau} + A_q p_{1,n}^{\tau} \\ \vdots \\ T_{m,n}^{\tau} + A_q p_{m,n}^{\tau} \\ T_{bath} \end{pmatrix}, \quad (\text{B15})$$

where the last row contains the equation $T_b = T_{bath}$ which is used to set the bath temperature as boundary condition.

The metal-insulator phase transition in V_2O_3 is connected to the occurrence of a latent heat of approximately $\Delta H = 2 \text{ kJ/mol} \approx 13.3 \text{ kJ/kg}$ that has to be supplied to the system to change from one phase to the other [55]. The latent heat, which is represented by a jump in enthalpy H , leads to a diverging heat capacity $c_P = dH/dT$ at the phase transition [56]. The latent heat is represented in the numerical model by introducing a temperature dependent heat capacity

$$c_P(T) = c_{P0} + \frac{\Delta H}{\sqrt{\pi} \Delta T} e^{-\frac{(T-T_c)^2}{\Delta T^2}}, \quad (\text{B16})$$

where a constant heat capacity $c_{P0} = 0.45 \text{ kJ/(kg K)}$ and a finite width $\Delta T = 0.1 \text{ K}$ of the phase transition around

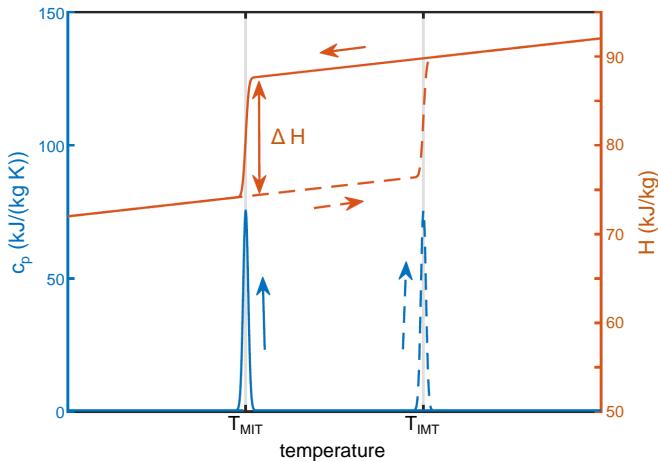


FIG. 11. Temperature dependent heat capacity c_P (blue curve) and enthalpy H (red curve). The latent heat ΔH at the phase transition leads to a jump in enthalpy and a peak in heat capacity. Broken lines show the IMT at T_{IMT} , solid lines the MIT at T_{MIT} .

the transition temperature T_c is assumed. The heat capacity according to Eq. (B16) is shown in Fig. 11.

4. Simulation of electric breakdown in V_2O_3

To simulate the electric breakdown in V_2O_3 , the equations for the current distribution and heat transfer [Eq. (B1) and Eq. (B15), respectively] are implemented and solved in MATLAB. This is done by initializing the system at zero bias current ($I_{\text{bias}} = 0$) and at the bath temperature ($T_{i,j} = T_{\text{bath}}$) for $t = 0$ and slowly ramping the current to $I_{\text{bias}}^{\text{max}} = 20 \text{ mA}$ and back to $I_{\text{bias}}^{\text{end}} = 0 \text{ mA}$ over time with a rate that is much slower than the thermal dynamics of the sample, so that the system is modeled in quasi-static approximation.

Figure 12 shows the programs flow chart. First, the system is initialized at the bath temperature, zero bias current and completely in the insulating phase. Then, the $R_{i,j}$ for the initial temperature and phase are calculated. The bias current is increased to the value at the next time step $t + \Delta t$. The mesh current analysis is solved and the current distribution is calculated. The Joule heating is calculated from $R_{i,j}$ and the current distribution and input into the heat equation, which is solved for the temperatures $T_{i,j}(t + \Delta t)$. Note that, due to the strong temperature dependence of resistivity and heat capacity, the system is highly nonlinear as it approaches the MIT or IMT. To accurately capture the nonlinearities a sufficiently small time step Δt needs to be used. This is accomplished by using an adaptive time

step. If the maximum change in temperature

$$\Delta T = \max_{i,j} (|T_{i,j}(t + \Delta t) - T_{i,j}(t)|) \quad (\text{B17})$$

is larger than the convergence criterion δ , the time step is

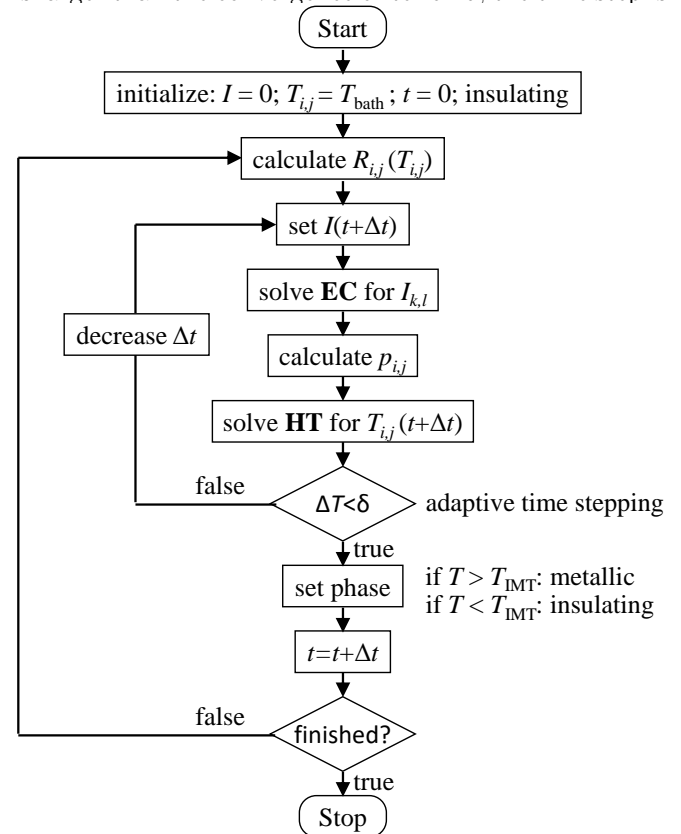
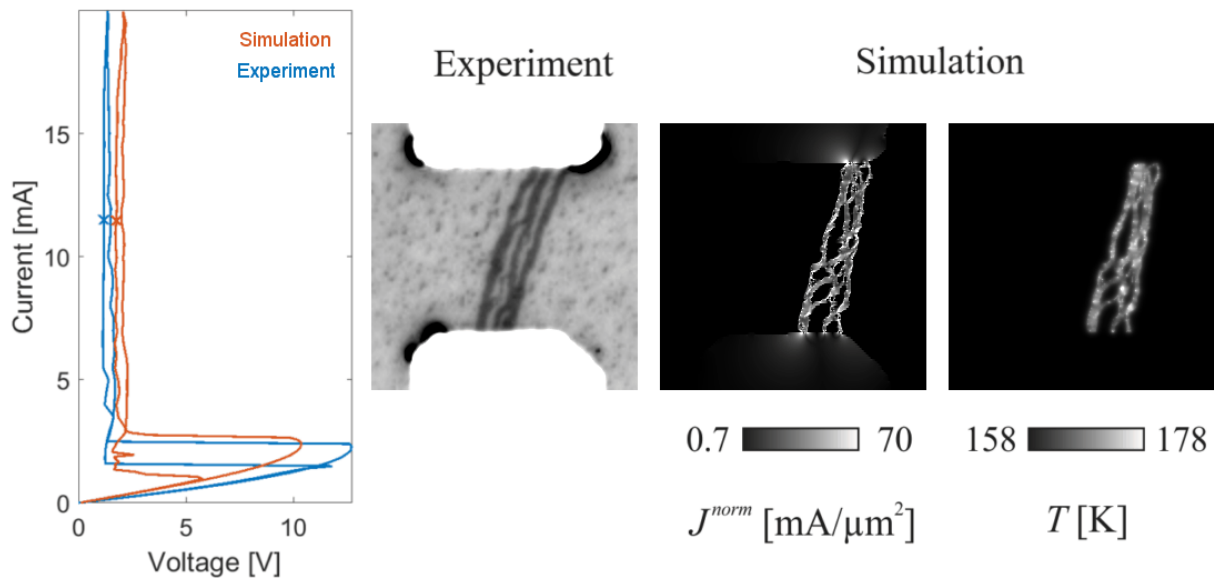


FIG. 12. Flow chart for the simulation.

reduced and the temperature distribution is recalculated using the smaller time step. If ΔT is far below the convergence criterion, the time step is increased. When the convergence criterion is satisfied, the phase transition is evaluated: the material is set to the metallic phase, where T_{IMT} is exceeded and to the insulating phase, where the temperature has fallen below T_{MIT} . Subsequently, the time is incremented and the calculated temperature and phase distribution are used as inputs to calculate the new $R_{i,j}$ values. The program runs in a loop, progressing through time, until the bias current has reached its final value.

Appendix C: Current-Voltage Relation, Photomicrographs and Computer Simulation Data Combined in One Animation

To summarize the main results on resistive switching due to electrothermal filament formation, we combined the electrical transport measurement data, the photomicrographs, and the computer simulation data in one animation (see Video 1).



Video 1. Animation of the electrical breakdown in a planar thin-film device at the onset of the IMT. The left graph shows the current-voltage relation of the experiment and the simulation. Two small “x” mark the bias points. The panel in the center shows the corresponding photomicrographs of the device under investigation. The two panel on the right show the simulated current density and temperature.

-
- [1] P. Limelette, A. Georges, D. Jérôme, P. Wzietek, P. Metcalf, and J. M. Honig, Universality and critical behavior at the Mott transition, *Science* **302**, 89 (2003).
- [2] D. B. McWhan and J. P. Remeika, Metal-insulator transition in $(V_{1-x}Cr_x)_2O_3$, *Phys. Rev. B* **2**, 3734 (1970).
- [3] M. Imada, A. Fujimori, and Y. Tokura, Metal-insulator transitions, *Rev. Mod. Phys.* **70**, 1039 (1998).
- [4] A. Singer, J. G. Ramirez, I. Valmianski, D. Cela, N. Hua, R. Kukreja, J. Wingert, O. Kovalchuk, J. M. Glownia, M. Sikorski, M. Chollet, M. Holt, I. K. Schuller, and O. G. Shpyrko, Nonequilibrium phase precursors during a photoexcited insulator-to-metal transition in V_2O_3 , *Phys. Rev. Lett.* **120**, 207601 (2018).
- [5] Z. Yang, C. Ko, and S. Ramanathan, Oxide electronics utilizing ultrafast metal-insulator transitions, *Annu. Rev. Mater. Res.* **41**, 337 (2011).
- [6] P. Markov, R. E. Marvel, H. J. Conley, K. J. Miller, R. F. Haglund, Jr., and S. M. Weiss, Optically monitored electrical switching in VO_2 , *ACS Photonics* **2**, 1175 (2015).
- [7] N. A. Butakov, I. Valmianski, T. Lewi, C. Urban, Z. Ren, A. A. Mikhailovsky, S. D. Wilson, I. K. Schuller, and J. A. Schuller, Switchable plasmonic-dielectric resonators with metal-insulator transitions, *ACS Photonics* **5**, 371 (2018).
- [8] J. del Valle, Y. Kalcheim, J. Trastoy, A. Charnukha, D. N. Basov, and I. K. Schuller, Electrically induced multiple metal-insulator transitions in oxide nanodevices, *Phys. Rev. Applied* **8**, 054041 (2017).
- [9] E. Janod, J. Tranchant, B. Corraze, M. Querré, P. Stolar, M. Rozenberg, T. Cren, D. Roditchev, V. T. Phuoc, M. Besland, and L. Cario, Resistive switching in Mott insulators and correlated systems, *Adv. Funct. Mater.* **25**, 6287 (2015).
- [10] C.-Y. Lin, P.-H. Chen, T.-C. Chang, K.-C. Chang, S.-D. Zhang, T.-M. Tsai, C.-H. Pan, M.-C. Chen, Y.-T. Su, Y.-T. Tseng, Y.-F. Chang, Y.-C. Chen, H.-C. Huang, and S. M. Sze, Attaining resistive switching characteristics and selector properties by varying forming polarities in a single HfO_2 -based RRAM device with a vanadium electrode, *Nanoscale* **9**, 8586 (2017).
- [11] A. Sawa, Resistive switching in transition metal oxides, *Mater. Today* **11**, 28 (2008).
- [12] H. S. P. Wong, H.-Y. Lee, S. Yu, Y.-S. Chen, Y. Wu, P.-S. Chen, B. Lee, F. T. Chen, and M.-J. Tsai, Metal-oxide RRAM, *Proceedings of the IEEE* **100**, 1951 (2012).
- [13] M. A. Zidan, J. P. Strachan, and W. D. Lu, The future of electronics based on memristive systems, *Nat. Electron.* **1**, 22 (2018).
- [14] D. Ielmini and H. S. P. Wong, In-memory computing with resistive switching devices, *Nat. Electron.* **1**, 333 (2018).
- [15] Z. Wang, H. Wu, G. W. Burr, C. S. Hwang, K. L. Wang, Q. Xia, and J. J. Yang, Resistive switching materials for information processing, *Nat. Rev. Mater.* **5**, 173 (2020).
- [16] M. D. Pickett, G. Medeiros-Ribeiro, and R. S. Williams, A scalable neuristor built with mott memristors, *Nat. Mater.* **12**, 114 (2013).

- [17] I. K. Schuller, R. Stevens, R. Pino, and M. Pechan, Neuromorphic computing – from materials research to systems architecture roundtable, DOI:10.2172/1283147 (2015).
- [18] P. Stoliar, J. Tranchant, B. Corraze, E. Janod, M. Besland, F. Tesler, M. Rozenberg, and L. Cario, A leaky-integrate-and-fire neuron analog realized with a Mott insulator, *Adv. Funct. Mater.* **27**, 1604740 (2017).
- [19] W. Yi, K. Tsang, S. Lam, X. Bai, J. Crowell, and E. Flores, Biological plausibility and stochasticity in scalable VO₂ active memristor neurons, *Nat. Commun.* **9**, 4661 (2018).
- [20] J. del Valle, P. Salev, F. Tesler, N. M. Vargas, Y. Kalcheim, P. Wang, J. Trastoy, M.-H. Lee, G. Kassabian, J. G. Ramírez, M. J. Rozenberg, and I. K. Schuller, Subthreshold firing in Mott nanodevices, *Nature* **569**, 388 (2019).
- [21] T. Oka, R. Arita, and H. Aoki, Breakdown of a Mott insulator: A nonadiabatic tunneling mechanism, *Phys. Rev. Lett.* **91**, 066406 (2003).
- [22] H. Yamakawa, T. Miyamoto, T. Morimoto, T. Terashige, H. Yada, N. Kida, M. Suda, H. M. Yamamoto, R. Kato, K. Miyagawa, K. Kanoda, and H. Okamoto, Mott transition by an impulsive dielectric breakdown, *Nat. Mater.* **16**, 1100 (2017).
- [23] T. Oka and H. Aoki, Ground-state decay rate for the Zener breakdown in band and Mott insulators, *Phys. Rev. Lett.* **95**, 137601 (2005).
- [24] M. Eckstein, T. Oka, and P. Werner, Dielectric breakdown of Mott insulators in dynamical mean-field theory, *Phys. Rev. Lett.* **105**, 146404 (2010).
- [25] F. Heidrich-Meisner, I. González, K. A. Al-Hassanieh, A. E. Feiguin, M. J. Rozenberg, and E. Dagotto, Nonequilibrium electronic transport in a one-dimensional Mott insulator, *Phys. Rev. B* **82**, 205110 (2010).
- [26] R. Kumai, Y. Okimoto, and Y. Tokura, Current-induced insulator-metal transition and pattern formation in an organic charge-transfer complex, *Science* **284**, 1645 (1999).
- [27] S. Yamanouchi, Y. Taguchi, and Y. Tokura, Dielectric breakdown of the insulating charge-ordered state in La_{2-x}Sr_xNiO₄, *Phys. Rev. Lett.* **83**, 5555 (1999).
- [28] I. Valmianski, P. Y. Wang, S. Wang, J. G. Ramírez, S. Guéron, and I. K. Schuller, Origin of the current-driven breakdown in vanadium oxides: Thermal versus electronic, *Phys. Rev. B* **98**, 195144 (2018).
- [29] W.-R. Lee and K. Park, Dielectric breakdown via emergent nonequilibrium steady states of the electric-field-driven Mott insulator, *Phys. Rev. B* **89**, 205126 (2014).
- [30] N. Sugimoto, S. Onoda, and N. Nagaosa, Field-induced metal-insulator transition and switching phenomenon in correlated insulators, *Phys. Rev. B* **78**, 155104 (2008).
- [31] G. Mazza, A. Amaricci, M. Capone, and M. Fabrizio, Field-driven Mott gap collapse and resistive switch in correlated insulators, *Phys. Rev. Lett.* **117**, 176401 (2016).
- [32] J. Li, C. Aron, G. Kotliar, and J. E. Han, Electric-field-driven resistive switching in the dissipative Hubbard model, *Phys. Rev. Lett.* **114**, 226403 (2015).
- [33] J. Duchene, M. Terrailon, P. Pailly, and G. Adam, Filamentary conduction in VO₂ coplanar thin-film devices, *Appl. Phys. Lett.* **19**, 115 (2003).
- [34] S. Guéron, S. Scharinger, S. Wang, J. G. Ramírez, D. Koelle, R. Kleiner, and I. K. Schuller, Electrical breakdown in a V₂O₃ device at the insulator-to-metal transition, *EPL* **101**, 57003 (2013).
- [35] J. S. Brockman, L. Gao, B. Hughes, C. T. Rettner, M. G. Samant, K. P. Roche, and S. S. P. Parkin, Subnanosecond incubation times for electric-field-induced metallization of a correlated electron oxide, *Nat. Nanotechnol.* **9**, 453 (2014).
- [36] V. I. Polozov, S. S. Maklakov, A. L. Rakhmanov, S. A. Maklakov, and V. N. Kisel, Blow-up overheating instability in vanadium dioxide thin films, *Phys. Rev. B* **101**, 214310 (2020).
- [37] A. V. Gurevich and R. G. Mints, Self-heating in normal metals and superconductors, *Rev. Mod. Phys.* **59**, 941 (1987).
- [38] F. Giorgianni, J. Sakai, and S. Lupi, Overcoming the thermal regime for the electric-field driven Mott transition in vanadium sesquioxide, *Nat. Commun.* **10**, 1159 (2019).
- [39] Y. Kalcheim, A. Camjayi, J. del Valle, P. Salev, M. Rozenberg, and I. K. Schuller, Non-thermal resistive switching in Mott insulator nanowires, *Nat. Commun.* **11**, 2985 (2020).
- [40] H. Schuler, S. Klimm, G. Weissmann, C. Renner, and S. Horn, Influence of strain on the electronic properties of epitaxial V₂O₃ thin films, *Thin Solid Films* **299**, 119 (1997).
- [41] N. Alyabyeva, J. Sakai, M. Bavencoffe, J. Wolfman, P. Limelette, H. Funakubo, and A. Ruyter, Metal-insulator transition in V₂O₃ thin film caused by tip-induced strain, *Appl. Phys. Lett.* **113**, 241603 (2018).
- [42] A. Ronchi, P. Homm, M. Menghini, P. Franceschini, F. Maccherozzi, F. Banfi, G. Ferrini, F. Cilento, F. Parmigiani, S. S. Dhesi, M. Fabrizio, J.-P. Locquet, and C. Giannetti, Early-stage dynamics of metallic droplets embedded in the nanotextured Mott insulating phase of V₂O₃, *Phys. Rev. B* **100**, 075111 (2019).
- [43] A. S. McLeod, E. van Heumen, J. G. Ramírez, S. Wang, T. Saerbeck, S. Guéron, M. Goldflam, L. Anderegg, P. Kelly, A. Mueller, M. K. Liu, I. K. Schuller, and D. N. Basov, Nanotextured phase coexistence in the correlated insulator V₂O₃, *Nat. Phys.* **13**, 80 (2017).
- [44] P. Stoliar, L. Cario, E. Janod, B. Corraze, C. Guillot-Deudon, S. Salmon-Bourmand, V. Guiot, J. Tranchant, and M. Rozenberg, Universal electric-field-driven resistive transition in narrow-gap Mott insulators, *Adv. Mater.* **25**, 3222 (2013).
- [45] P. Diener, E. Janod, B. Corraze, M. Querré, C. Adda, M. Guilloux-Viry, S. Cordier, A. Camjayi, M. Rozenberg, M. P. Besland, and L. Cario, How a dc electric field drives Mott insulators out of equilibrium, *Phys. Rev. Lett.* **121**, 016601 (2018).
- [46] G. Gopalakrishnan, D. Ruzmetov, and S. Ramanathan, On the triggering mechanism for the metal-insulator transition in thin film VO₂ devices: electric field versus thermal effects, *J. Mater. Sci.* **44**, 5345 (2009).
- [47] A. Ronchi, P. Franceschini, P. Homm, M. Gandolfi, G. Ferrini, S. Pagliara, F. Banfi, M. Menghini, J.-P. Locquet, and C. Giannetti, Light-assisted resistance collapse in a V₂O₃-based Mott-insulator device, *Phys. Rev. Applied* **15**, 044023 (2021).
- [48] M. K. Stewart, D. Brownstead, S. Wang, K. G. West, J. G. Ramirez, M. M. Qazilbash, N. B. Perkins, I. K. Schuller, and D. N. Basov, Insulator-to-metal transition and correlated metallic state of V₂O₃ investigated by optical spectroscopy, *Phys. Rev. B* **85**, 205113 (2012).

- [49] M. Lange, S. Guénon, F. Lever, R. Kleiner, and D. Koelle, A high-resolution combined scanning laser- and widefield polarizing microscope for imaging at temperatures from 4 K to 300 K, *Rev. Sci. Instr.* **88**, 123705 (2017).
- [50] A. I. Poteryaev, J. M. Tomczak, S. Biermann, A. Georges, A. I. Lichtenstein, A. N. Rubtsov, T. Saha-Dasgupta, and O. K. Andersen, Enhanced crystal-field splitting and orbital-selective coherence induced by strong correlations in V_2O_3 , *Phys. Rev. B* **76**, 085127 (2007).
- [51] S.-K. Mo, J. D. Denlinger, H.-D. Kim, J.-H. Park, J. W. Allen, A. Sekiyama, A. Yamasaki, K. Kadono, S. Suga, Y. Saitoh, T. Muro, P. Metcalf, G. Keller, K. Held, V. Eyert, V. I. Anisimov, and D. Vollhardt, Prominent quasi-particle peak in the photoemission spectrum of the metallic phase of V_2O_3 , *Phys. Rev. Lett.* **90**, 186403 (2003).
- [52] See Supplemental Material at [URL] for further details on the phase separation at the MIT/IMT, on the description of the numerical model and for measured IVC, photomicrographs, and simulation data of the electrical breakdown in a planar V_2O_3 device combined in one animation.
- [53] H. Garcke and U. Weikard, Numerical approximation of the Cahn-Larché equation, *Numer. Math.* **100**, 639 (2005).
- [54] M. Lange, *A High-Resolution Polarizing Microscope for Cryogenic Imaging: Development and Application to Investigations on Twin Walls in $SrTiO_3$ and the Metal-Insulator Transition in V_2O_3* , Ph.D. thesis, Eberhard Karls Universität Tübingen (2018), DOI:10.15496/publikation-26825.
- [55] H. V. Keer, D. L. Dickerson, H. Kuwamoto, H. L. C. Barros, and J. M. Honig, Heat capacity of pure and doped V_2O_3 single crystals, *J. Solid State Chem.* **19**, 95 (1976).
- [56] O. V. Lyakh, V. I. Surikov, V. I. Surikov, and N. A. Prokudina, Magnetic susceptibility and heat capacity of V_2O_3 and $V_{1.973}Me_{0.020}O_3$ (Me = Fe, Cr and Al), *Russ. Phys. J* **55**, 116 (2012).